UCSF

Title

GLUT3 upregulation promotes metabolic reprogramming associated with antiangiogenic therapy resistance

Permalink

Journal

ISSN

Authors

Kuang, Ruby
Jahangiri, Arman
Mascharak, Smita
et al.

Publication Date

DOI

Peer reviewed

JCI insight

GLUT3 upregulation promotes metabolic reprogramming associated with antiangiogenic therapy resistance

Ruby Kuang,[1] Arman Jahangiri,[1] Smita Mascharak,[1] Alan Nguyen,[1] Ankush Chandra,[1] Patrick M. Flanigan,[1] Garima Yagnik,[1] Jeffrey R. Wagner,[1] Michael De Lay,[1] Diego Carrera,[1] Brandyn A. Castro,[1] Josie Hayes,[1] Maxim Sidorov,[1] Jose Luiz Izquierdo Garcia,[2] Pia Eriksson,[2] Sabrina Ronen,[2] Joanna Phillips,[3] Annette Molinaro,[1] Suneil Koliwad,[4] and Manish K. Aghi[1]

[1]Department of Neurological Surgery, [2]Department of Radiology, [3]Department of Neuropathology, and [4]Diabetes Center, University of California at San Francisco, San Francisco, California, USA.

Clinical trials revealed limited response duration of glioblastomas to VEGF-neutralizing antibody bevacizumab. Thriving in the devascularized microenvironment occurring after antiangiogenic therapy requires tumor cell adaptation to decreased glucose, with 50% less glucose identified in bevacizumab-treated xenografts. Compared with bevacizumab-responsive xenograft cells, resistant cells exhibited increased glucose uptake, glycolysis, ^{13}C NMR pyruvate to lactate conversion, and survival in low glucose. Glucose transporter 3 (GLUT3) was upregulated in bevacizumab-resistant versus sensitive xenografts and patient specimens in a HIF-1α–dependent manner. Resistant versus sensitive cell mitochondria in oxidative phosphorylation–selective conditions produced less ATP. Despite unchanged mitochondrial numbers, normoxic resistant cells had lower mitochondrial membrane potential than sensitive cells, confirming poorer mitochondrial health, but avoided the mitochondrial dysfunction of hypoxic sensitive cells. Thin-layer chromatography revealed increased triglycerides in bevacizumab-resistant versus sensitive xenografts, a change driven by mitochondrial stress. A glycogen synthase kinase-3β inhibitor suppressing GLUT3 transcription caused greater cell death in bevacizumab-resistant than -responsive cells. Overexpressing GLUT3 in tumor cells recapitulated bevacizumab-resistant cell features: survival and proliferation in low glucose, increased glycolysis, impaired oxidative phosphorylation, and rapid in vivo proliferation only slowed by bevacizumab to that of untreated bevacizumab-responsive tumors. Targeting GLUT3 or the increased glycolysis reliance in resistant tumors could unlock the potential of antiangiogenic treatments.

Introduction

Antiangiogenic therapies such as the VEGF-neutralizing antibody bevacizumab hold promise for the treatment of malignancies such as glioblastoma, a devastating brain cancer for which effective treatments are gravely needed. However, while the initial responses to antiangiogenic therapy are often significant, these agents have limited durations of response (1). Half of glioblastomas treated with bevacizumab acquire therapeutic resistance after an initial response (2). Acquired resistance to antiangiogenic therapy creates tumors we have found to have a poor prognosis (3, 4), owing to these resistant tumors exhibiting both increased invasiveness and increased proliferation (3), making it a significant problem and preventing these treatments from fulfilling their therapeutic promise.

We (3, 5) and others (6) have found that increased hypoxia is a defining feature of tumors resistant to antiangiogenic therapy. We have previously reported hypoxia-induced autophagy as a mechanism by which tumors resistant to antiangiogenic therapy survive the hypoxia induced by these treatments (5). However, the ability of these resistant tumors to thrive in the harsh microenvironment created by antiangiogenic therapy requires that they not only survive hypoxia but also metabolically adapt to the decreased availability of glucose (7) that has been described after antiangiogenic therapy in order to achieve the increased proliferation we have described in these resistant tumors (3). As such, we investigated the hypothesis that a metabolic reprogramming towards more efficient glucose uptake and a more glycolytic phenotype with

lesser mitochondrial capacity for oxidative phosphorylation occurs during the evolution of resistance to antiangiogenic therapy. In seeking to identify specific mediators of these changes, we found upregulation of GLUT3 to occur in 2 xenograft models of bevacizumab resistance and in patient specimens from bevacizumab-resistant glioblastomas, with GLUT3 promoting metabolic features of bevacizumab resistance in a targetable manner.

Results

Cells from a bevacizumab-resistant xenograft model shift towards glycolysis compared with cells from a paired isogenic responsive xenograft model. Using a colorimetric assay, we confirmed that 4 weeks of bevacizumab treatment of subcutaneous U87 glioma cell line–derived xenografts lowered glucose levels in the tumor tissue more than 2-fold compared with IgG-treated xenografts ($P = 0.03$; Figure 1A). We then investigated whether bevacizumab resistance was associated with a compensatory increase in the efficiency of glucose uptake to adapt to this treatment-induced low glucose microenvironment. To do so, we analyzed U87-Bev^S and U87-Bev^R, isogenic xenograft models of bevacizumab sensitivity versus resistance that we developed by serial multigenerational treatment of U87 xenografts with either bevacizumab or a control IgG antibody (8, 9). We found 50% more glucose uptake in freshly isolated cultured cells from bevacizumab-resistant U87-Bev^R versus sensitive U87-Bev^S xenografts, both under normoxic ($P = 0.03$) and hypoxic ($P = 0.03$) conditions (Figure 1B). To determine whether this adaptive increase in glucose uptake was associated with changes in glycolysis, we used a Seahorse extracellular flux analyzer to dynamically assess extracellular acidification as a measure of glycolysis in freshly isolated cells from U87-Bev^R versus U87-Bev^S xenografts. U87-Bev^R cells exhibited the same baseline extracellular acidification as U87-Bev^S cells ($P = 0.1$–0.2). However, once stressed by inhibitors of mitochondrial oxidative phosphorylation, U87-Bev^R cells exhibited greater extracellular acidification than U87-Bev^S, consistent with greater stress-associated glycolysis (range: $P < 0.001$ to $P = 0.03$; Figure 1C). Similarly, a colorimetric assay to measure glycolysis by detecting pyruvate production revealed no differences in pyruvate production between U87-Bev^R cells versus U87-Bev^S cells in normoxia ($P = 0.2$), but increased pyruvate production in U87-Bev^R cells versus U87-Bev^S cells under the stress of hypoxia ($P = 0.008$) (Figure 1D). Additional evidence supporting increased glycolysis in cells from bevacizumab-resistant xenografts came from ^{13}C NMR spectroscopic measurements, showing increased pyruvate to lactate conversion in U87-Bev^R relative to U87-Bev^S cells (Figure 1E). Consistent with this evidence supporting increased capacity to upregulate glycolysis under stress, U87-Bev^R cells produced more ATP than U87-Bev^S cells in 4.5 g/l glucose and normoxia ($P = 0.03$), a significant tendency that persisted with hypoxia (1% oxygen) ($P = 0.03$) (Figure 1F).

GLUT3 is upregulated in paired isogenic bevacizumab-resistant versus -sensitive xenografts in a HIF-1α–dependent manner. Using Western blots, we characterized expression of 7 key sequential regulatory points in glycolysis and their associated significant isoforms in U87-Bev^R versus U87-Bev^S subcutaneous xenografts: GLUT1 and GLUT3; hexokinase isoforms 1, 2, and 3 (HK1, HK2, and HK3), phosphofructokinase (PFK), pyruvate kinase isoform M2 (PK-M2), lactate dehydrogenase (LDH), pyruvate dehydrogenase (PDH), and pyruvate dehydrogenase kinase isoform 2 (PDK2). Of these 7 key regulatory points, only the GLUT3 ($P = 0.008$) isoform of GLUT and LDH ($P = 0.008$) were upregulated in subcutaneous U87-Bev^R xenografts relative to U87-Bev^S xenografts, while HK3 was downregulated ($P = 0.03$) (Figure 2A and Supplemental Figures 1 and 2; supplemental material available online with this article; doi:10.1172/jci.insight.88815DS1). The increased GLUT3 expression we noted in bevacizumab-resistant U87-Bev^R xenografts relative to bevacizumab-responsive U87-Bev^S xenografts was consistent with the increased glucose uptake we demonstrated in the resistant cells (Figure 1B), while the increased LDH expression we noted in U87-Bev^R xenografts relative to U87-Bev^S xenografts was consistent with the increased glycolytic flux noted in the resistant cells (Figure 1C).

We further analyzed GLUT3 expression in intracranial U87-Bev^R and U87-Bev^S xenografts treated with control IgG antibody or bevacizumab, and found by Western blot that bevacizumab increased GLUT3 expression in only U87-Bev^R xenografts ($P = 0.03$) (Figure 2B) and that bevacizumab increased intratumoral glucose in U87-Bev^R xenografts (Supplemental Figure 3), confirming a functional impact of the GLUT3 upregulation occurring in the resistant xenografts. To identify a potential regulator of GLUT3 expression, we analyzed HIF-1α expression by Western blot in these intracranial xenograft groups and found that bevacizumab lowered HIF-1α expression in U87-Bev^S xenografts ($P = 0.03$). Bevacizumab tended to increase HIF-1α expression in U87-Bev^R xenografts, although this tendency did not reach significance
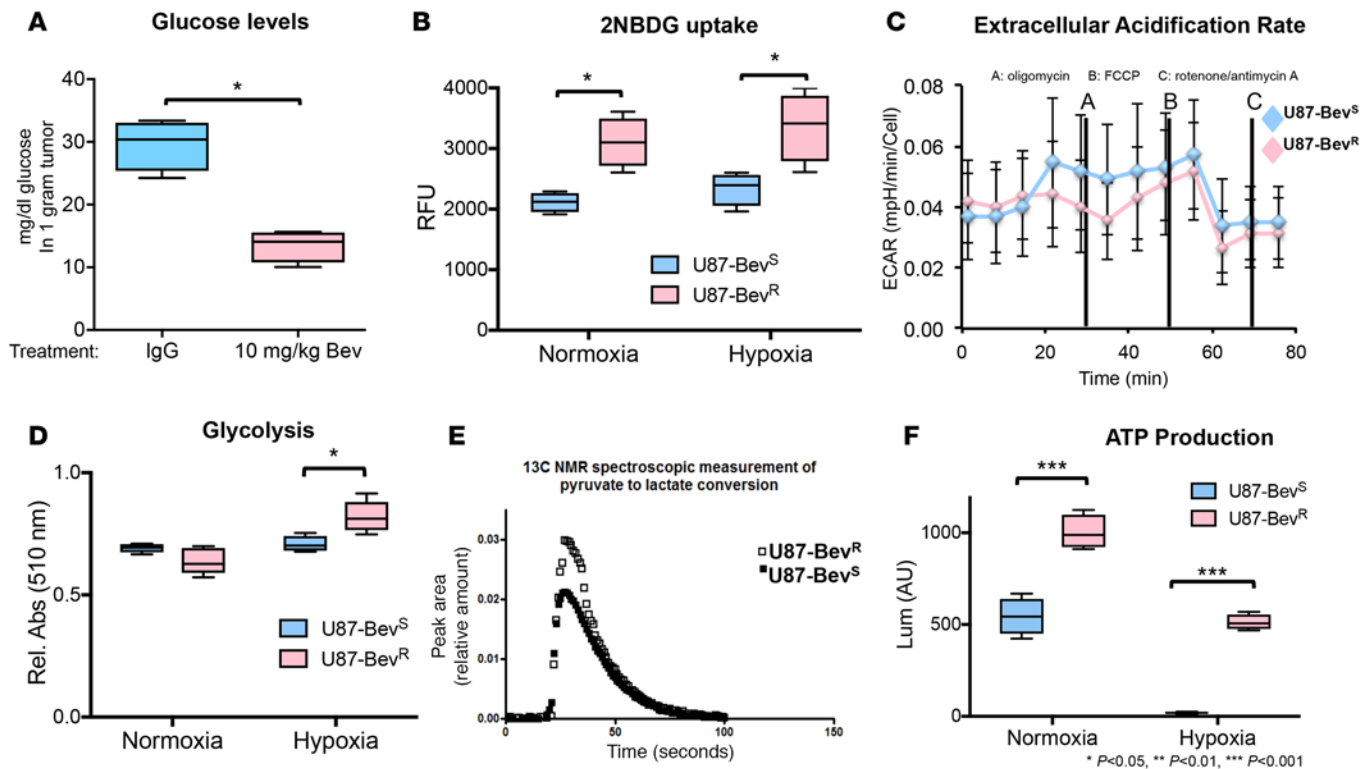
Figure 1. Increased glycolytic metabolism in a xenograft model of antiangiogenic therapy resistance. (**A**) Bevacizumab treatment (10 mg/kg twice per week until volumetric endpoint reached) lowered intratumoral glucose compared with IgG control antibody treatment of subcutaneous U87 xenografts. $P = 0.03$, Wilcoxon-Mann-Whitney test, $n = 4$ replicates/group. (**B**) Cultured bevacizumab-resistant glioma cell line–derived xenograft (U87-Bev[R]) cells exhibited more glucose uptake than cultured bevacizumab-sensitive (U87-Bev[S]) cells in normoxia ($P = 0.03$) and hypoxia ($P = 0.03$). Wilcoxon-Mann-Whitney test, $n = 4$ replicates/group. 2NBDG, fluorescently labeled deoxyglucose analog. (**C**) Cultured U87-Bev[R] cells exhibited the same baseline extracellular acidification rate (ECAR) as U87-Bev[S] cells ($P = 0.1$–0.2, Wilcoxon-Mann-Whitney test), but greater ECAR when treated with inhibitors of mitochondrial oxidative phosphorylation, consistent with greater stress-associated glycolysis (range: $P < 0.001$ to $P = 0.03$, Wilcoxon-Mann-Whitney test). $n = 46$ samples/cell type/time point. (**D**) Cultured U87-Bev[R] cells produced more pyruvate than U87-Bev[S] cells in hypoxia ($P = 0.008$) but not normoxia ($P = 0.2$). Wilcoxon-Mann-Whitney test, $n = 5$ replicates/group. (**E**) ^{13}C NMR spectroscopic measurement of pyruvate to lactate conversion revealed greater conversion in U87-Bev[R] relative to U87-Bev[S]. (**F**) ATP production assessed by a chemiluminescence assay revealed U87-Bev[R] to produce more ATP production than U87-Bev[S] in normoxic cells in DMEM ($P = 0.03$), with the difference persisting in hypoxia ($P = 0.03$). Wilcoxon-Mann-Whitney test, $n = 4$ replicates/group. For ECAR curves, error bars represent SDs. For box-and-whisker plots, the horizontal line in the box is the median, while the box extends from the 25th to 75th percentile and the whiskers from minimum to maximum values. *$P < 0.05$ and ***$P < 0.001$.

($P = 0.1$; Figure 2B and Supplemental Figure 4). We investigated the relationship between HIF-1α and the increased GLUT3 expression in bevacizumab-resistant xenografts further by treating cultured U87-Bev[S] and U87-Bev[R] xenograft-derived cells with YC-1, a nitric oxide–independent activator of soluble guanylyl cyclase that inhibits HIF-1α at the posttranslational level. YC-1 lowered GLUT3 protein expression in hypoxic U87-Bev[R] cells and in normoxic U87-Bev[S] cells (Figure 2C), but did not alter GLUT1 expression (Supplemental Figure 5). We then performed HIF-1α and GLUT3 costaining of intracranial U87-Bev[R] and U87-Bev[S] xenografts. We found that bevacizumab decreased HIF-1α expression in U87-Bev[S] xenografts ($P = 0.0081$) without changing GLUT3 expression ($P = 0.36$), but, consistent with the Western blot results, increased HIF-1α ($P = 0.0083$) and GLUT3 ($P = 0.0082$) expression in U87-Bev[R] xenografts (Figure 3). Spatial correlation between HIF-1α and GLUT3 expression (Figure 3) was consistent with the HIF-1α regulation of GLUT3 supported by the HIF-1α inhibitor study.

GLUT3 is upregulated in bevacizumab-resistant patient-derived xenografts and patient glioblastomas. To support our findings in U87-Bev[R] and U87-Bev[S] xenografts in a more translational context, we performed HIF-1α and GLUT3 costaining of intracranial patient-derived bevacizumab-sensitive versus -resistant xenografts whose establishment and maintenance of the bevacizumab responsiveness of their corresponding patient tumor we have previously described (8, 10). When treating bevacizumab-responsive patient-derived intracranial SF7300 and GBM43 xenografts, we found that bevacizumab did not alter HIF-1α ($P = 0.9$ for SF7300 and $P = 0.3$ for GBM43) staining and did not alter ($P = 0.5$, SF7300) or lowered ($P = 0.03$, GBM43)
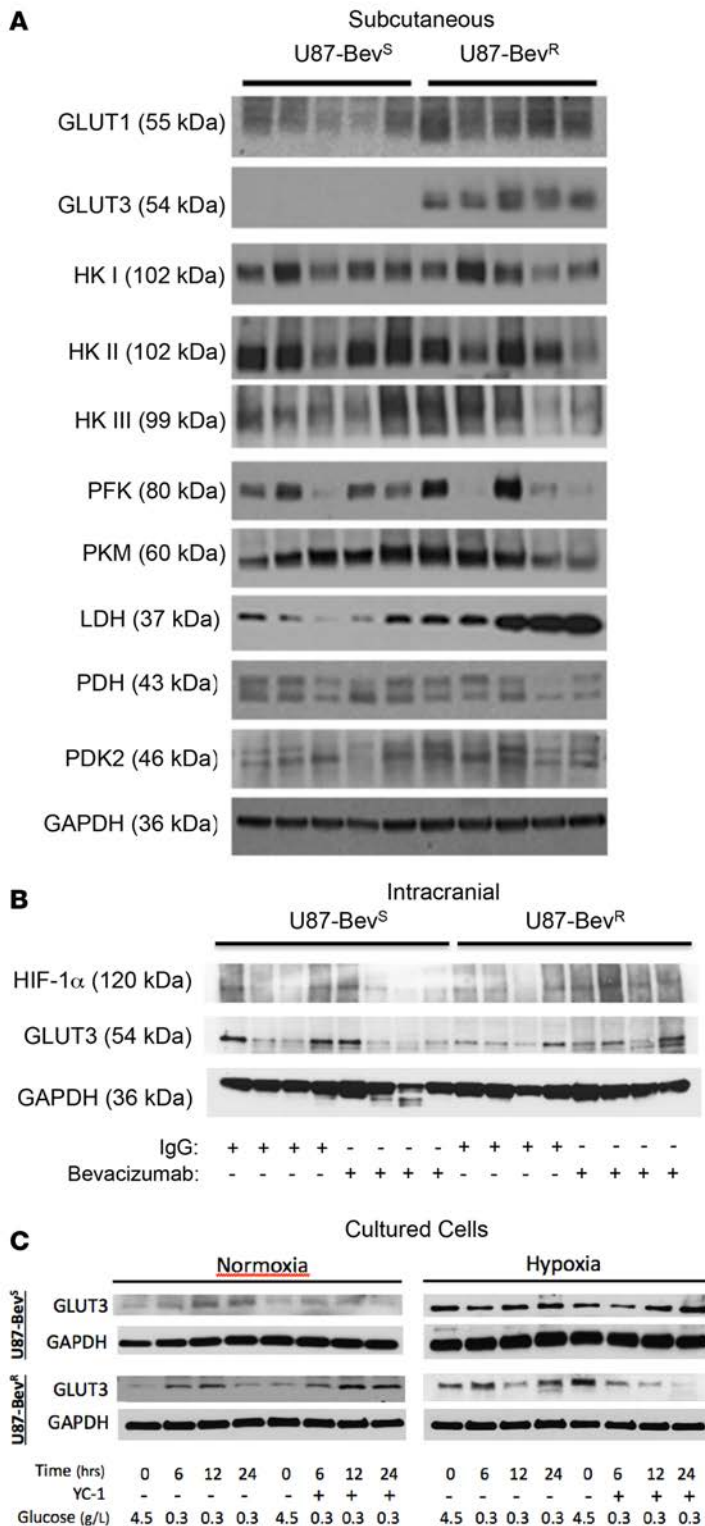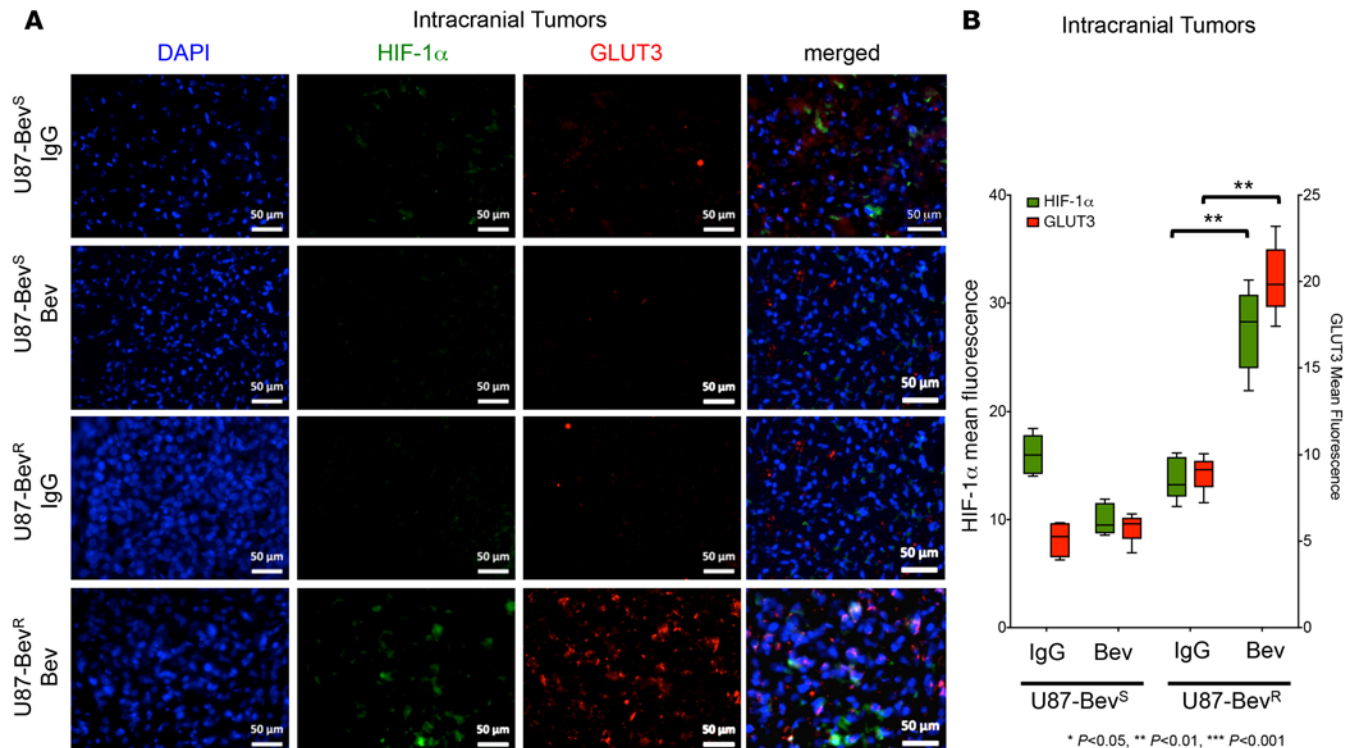
Figure 2. Increased GLUT3 expression in bevacizumab-resistant xenografts in a HIF-1α–dependent manner. (**A**) Among glycolytic enzymes and regulatory factors, Western blot revealed increased GLUT3, increased lactate dehydrogenase (LDH), and decreased HK3 in bevacizumab-resistant glioma cell line–derived xenograft (U87-Bev[R]) cells as the only significant changes (see Supplemental Figure 1 for quantification and statistical analysis) occurring between subcutaneous U87-Bev[R] vs. bevacizumab-sensitive (U87-Bev[S]) xenografts (*n* = 5 of each xenograft). Band sizes are indicated next to each lane. (**B**) By Western blot, bevacizumab increased GLUT3 expression in intracranial U87-Bev[R], not U87-Bev[S], xenografts. Bevacizumab lowered HIF-1α expression in intracranial U87-Bev[S] xenografts. Bevacizumab tended to increase HIF-1α expression in intracranial U87-Bev[R] xenografts, but this tendency did not reach significance (see Supplemental Figure 4 for quantification and statistical analysis). (**C**) Treatment of cultured U87-Bev[S] and U87-Bev[R] cells with 10 μM YC-1 (HIF-1α inhibitor) lowered GLUT3 protein expression in hypoxic U87-Bev[R] cells and in normoxic U87-Bev[S] cells.

GLUT3 staining (Figure 4, A and B, and Supplemental Figure 6). In contrast, when treating bevacizumab-resistant intracranial patient-derived SF7796 xenografts, bevacizumab increased HIF-1α (*P* = 0.03) and GLUT3 (*P* = 0.008) expression, with colocalized staining (Figure 4, A and B). We also found that, consistent with the GLUT3 expression results, bevacizumab decreased intratumoral glucose in GBM43 bevacizumab-responsive xenografts (*P* = 0.03; Figure 4C), while bevacizumab increased intratumoral glucose in SF7796 bevacizumab-resistant xenografts (*P* = 0.03; Figure 4C), confirming a functional impact of the GLUT3 upregulation occurring in the resistant patient-derived xenografts.

To analyze this phenomenon in patient glioblastomas, we obtained site-directed biopsies from the central core, enhancing edge, and infiltrated white matter of bevacizumab-resistant (*n* = 3) versus bevacizumab-naive glioblastomas (*n* = 5) and found increases in GLUT3 transcript copy number in each region of resistant tumors (*P* = 0.04 for each region; Figure 5A). This finding in patient glioblastomas was supported at the protein level when immunostaining revealed 8-fold more GLUT3 in bevacizumab-resistant patient glioblastomas compared with before treatment (*n* = 5), with no change in bevacizumab-naive glioblastomas at recurrence compared with at diagnosis (*n* = 5) (*P* = 0.008) (Figure 5, B and C).

Cells from bevacizumab-resistant xenografts exhibit decreased mitochondrial oxidative phosphorylation. We then investigated whether the increased capacity for glycolysis in bevacizumab-resistant cells was associated with alterations in their mitochondrial oxidative phosphorylation capability. Flow cytometry of cells stained with the mitochondrial dye MitoTracker revealed no significant difference in the number of mitochondria between U87-Bev[R] and U87-Bev[S] cells (*P* = 0.07; Figure 6A). We then assessed the mitochondrial health of these cells by incubating the cells with the fluorochrome JC-1 and calculating the red-to-green ratio, which increases with mitochondrial membrane potential; a higher red-to-green ratio indicates better mitochondrial health. Mitochondrial membrane potential was higher in U87-Bev[S] cells than U87-Bev[R] cells in normoxia (*P* = 0.03) (Figure 6B). Whereas hypoxia impaired mitochondrial function in both U87-Bev[S] and U87-Bev[R] cells as expected (*P* = 0.03) (Figure 6B), normoxic U87-Bev[R] cells had a remarkably reduced membrane potential, on par with hypoxic U87-Bev[S] cells (*P* =

Figure 3. Increased GLUT3 expression in isogeneic bevacizumab-resistant xenografts. (**A**) Immunostaining of intracranial xenografts (n = 5/group) and (**B**) quantification of the immunostaining intensity revealed decreased HIF-1α staining in bevacizumab- versus IgG-treated bevacizumab-sensitive glioma cell line–derived xenograft (U87-Bev^S) (P = 0.008) and increased HIF-1α (P = 0.008) and GLUT3 (P = 0.008) staining in bevacizumab- versus IgG-treated bevacizumab-resistant (U87-Bev^R) cells (Wilcoxon-Mann-Whitney test). Magnification, ×20. Scale bars: 50 μm. For the box-and-whisker plot, the horizontal line in the box is the median, while the box extends from the 25th to 75th percentile and the whiskers from minimum to maximum values. **P < 0.01.

0.2), indicating the level of mitochondrial impairment in cells from bevacizumab-resistant xenografts. We then used the Seahorse extracellular flux analyzer to dynamically assess oxygen consumption as a measure of oxidative phosphorylation in freshly isolated cells from bevacizumab-resistant U87-Bev^R versus responsive U87-Bev^S xenografts. By assessing oxygen consumption rates in response to several electron transport inhibitors, we found that U87-Bev^R exhibited less basal respiration (P = 0.03) and less ATP production (P = 0.008) than did U87-Bev^S cells, confirming the baseline mitochondrial functional impairment suggested by our assessment of mitochondrial membrane potential. This oxygen consumption rate analysis did not reveal differences in spare respiratory capacity (P = 0.8) or proton leak (P = 0.3) between resistant versus responsive cells (Figure 6C and Supplemental Figure 7), suggesting that the baseline mitochondrial impairment of resistant cells did not affect their inner mitochondrial membrane permeability or their maximal capacity for ATP production when fully stressed. To further support this evidence for decreased baseline oxidative phosphorylation associated with bevacizumab resistance, we isolated mitochondria from U87-Bev^R and U87-Bev^S cells and grew them in 10 mM galactose and normoxia (20% oxygen), conditions that select for oxidative phosphorylation. Mitochondria from U87-Bev^R in these conditions produced less ATP than mitochondria from an equivalent number of U87-Bev^S cells (P = 0.03), a difference that was eliminated in hypoxia (P = 0.1) (Figure 6D). We further characterized mitochondrial changes noted in bevacizumab-resistant cells by analyzing the expression of mitochondrial enzymes COX IV, cytochrome C, and HSP60 in U87-Bev^R and U87-Bev^S xenografts. Of these 3 enzymes, only expression of HSP60, a heat shock protein involved in maintenance of oxidative phosphorylation (11) was altered, with decreased HSP60 protein noted in subcutaneous U87-Bev^R xenografts relative to subcutaneous U87-Bev^S xenografts (P = 0.02; Figure 6E and Supplemental Figure 8A), and quantitative real-time PCR (qPCR) showing confirmatory transcriptional changes (P = 0.003; Supplemental Figure 8B).

Bevacizumab-resistant xenografts have increased glycerolipid content with an increased ability to oxidize endogenous fatty acids under stress. Given that the balance between cellular oxidative and glycolytic metabolism is linked to
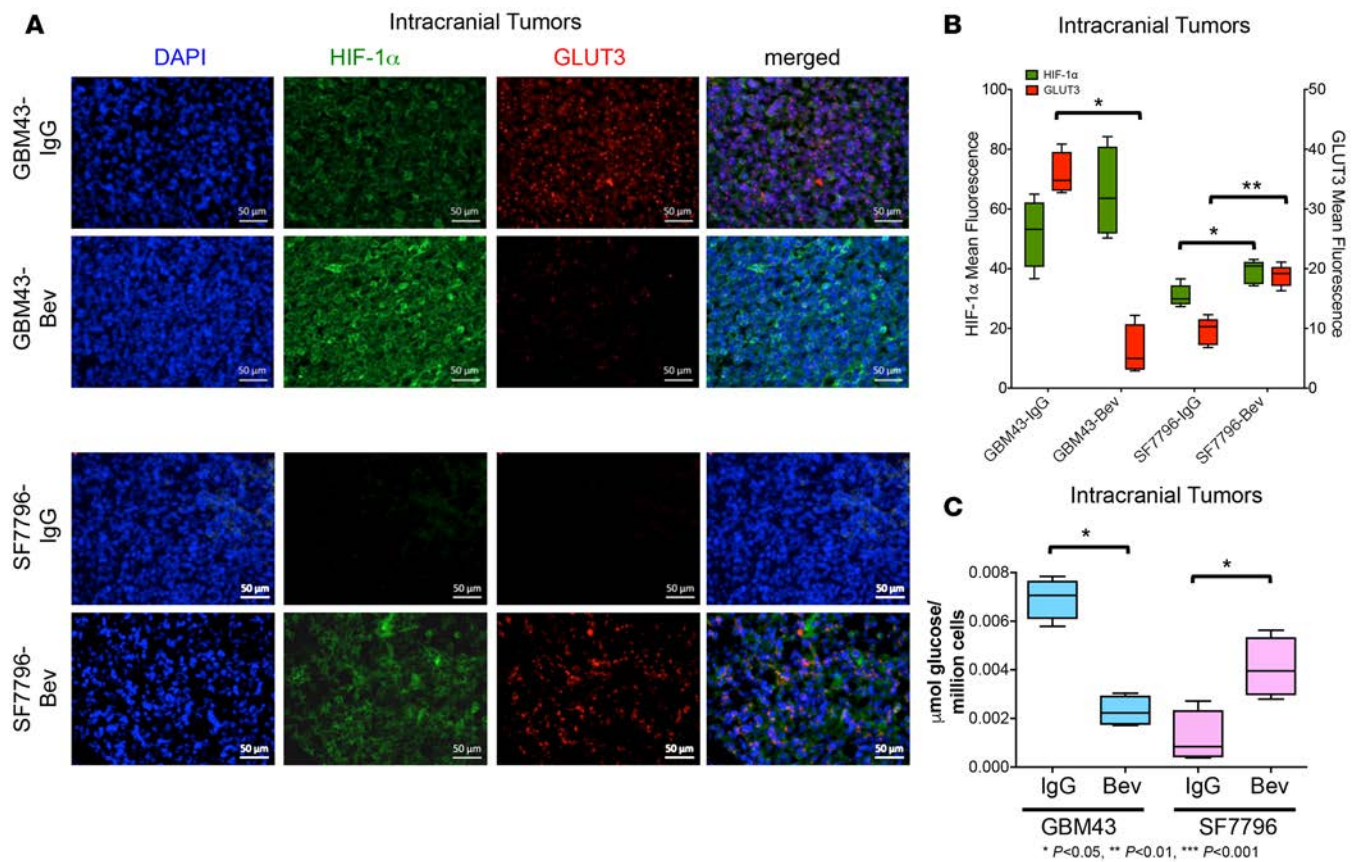
Figure 4. Increased GLUT3 expression in bevacizumab-resistant patient-derived xenografts. (A) Immunostaining of intracranial patient-derived xeno-grafts (PDXs) and **(B)** quantification of the immunostaining revealed that bevacizumab did not alter HIF-1α (*P* = 0.3) and lowered GLUT3 (*P* = 0.03) expression in bevacizumab-responsive GBM43 PDXs but increased HIF-1α (*P* = 0.04) and GLUT3 (*P* = 0.006) expression (Wilcoxon-Mann-Whitney test), with colocalized staining, in bevacizumab-resistant SF7796 PDXs. Magnification, ×20. Scale bars: 50 μm. **(C)** Glucose assay revealed that bevacizumab treatment decreased tumoral glucose in responsive GBM43 PDXs (*P*=0.03), but increased glucose in resistant SF7796 PDXs (*P* = 0.03). Wilcoxon-Mann Whitney test, *n* = 4/group. For box-and-whisker plots, the horizontal line in the box is the median, while the box extends from the 25th to 75th percentile and the whiskers from minimum to maximum values. **P* < 0.05, ***P* < 0.01.

lipid homeostasis, we then asked whether the metabolic changes described above for U87-Bev^R cells affects intracellular lipid levels in bevacizumab-resistant xenografts. Oil Red O, a dye that stains neutral lipids, including triglycerides, revealed increased staining in bevacizumab-resistant subcutaneous (*P* = 0.03) (Figure 7A) and intracranial (*P* = 0.003) (Figure 7B) xenografts. Thin-layer chromatography (TLC), which simultaneously measures relative levels of a variety of neutral lipids, was then used to further analyze these changes in bevacizumab-resistant glioblastoma xenografts in the orthotopic intracranial microenvironment. TLC revealed increased levels of triglycerides (*P* = 0.009) and decreased cholesterol (*P* = 0.002), with unchanged free fatty acids (*P* = 0.4), in U87-Bev^R xenografts compared with U87-Bev^S xenografts (Figure 7C). We then sought to determine whether hypoxia in the tumor microenvironment of bevacizumab-resistant tumors or the mitochondrial stress noted in bevacizumab-resistant xenograft cells were sources of the increased triglycerides noted in resistant xenografts. An AdipoRed assay revealed that mitochondrial stress from oxidative phosphorylation inhibitors (*P* = 0.004; Figure 7D), but not hypoxia (*P* = 0.6; Supplemental Figure 9), increased intracellular triglycerides in U87 cells. We then investigated whether the increased triglyceride levels in bevacizumab-resistant xenografts were associated with alterations in fatty acid biosynthesis or metabolism. We found no changes in the levels of assessed fatty acid synthesis enzymes fatty acid synthase, ACSL1, and phosphorylated and total acetyl-CoA carboxylase (ACC) between U87-Bev^R and U87-Bev^S xenografts (Figure 7E). We then examined fatty acid oxidative metabolism in cells from bevacizumab-resistant versus -responsive xenografts by using a Seahorse extracellular flux analyzer and the fatty acid oxidation inhibitor etomoxir to isolate the contribution of fatty acid oxidative metabolism to the basal respiration of each cell
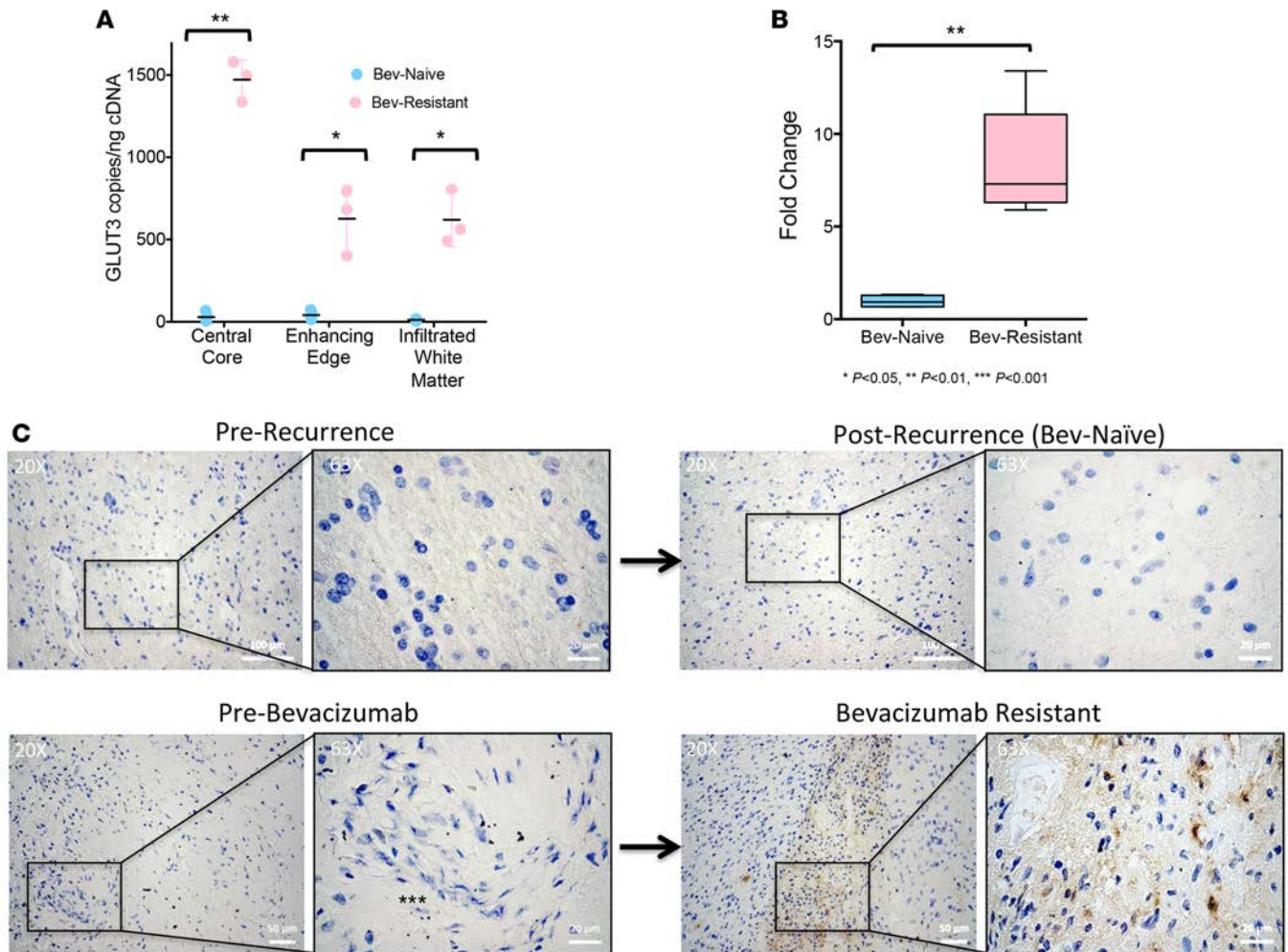
Figure 5. Increased GLUT3 expression in bevacizumab-resistant patient specimens. (A) Absolute quantification PCR revealed increased GLUT3 transcript levels in all regions of patient bevacizumab-resistant glioblastomas ($n = 3$) compared with bevacizumab-naive glioblastomas ($n = 5$) ($P < 0.001$). For the dot plot, the horizontal line represents the mean and vertical line represents the SD. **(B)** Quantification of immunostaining of patient glioblastomas revealed 8-fold more GLUT3 in bevacizumab-resistant patient glioblastomas compared with before treatment ($n = 5$), with no change in bevacizumab-naive glioblastomas at recurrence compared with at diagnosis ($n = 5$). $P = 0.008$, paired Student's t test. **(C)** Shown are representative images from each group at ×20 magnification (scale bars: 100 μm) with ×63 zoom (scale bars: 20 μm). For the box-and-whisker plot, the horizontal line in the box is the median, while the box extends from the 25th to 75th percentile and the whiskers from minimum to maximum values. *$P < 0.05$, **$P < 0.01$.

type. We found that the basal respiration due to oxidation of endogenous fatty acids in unstressed, normoxic cells was 18-fold higher in U87-Bev[R] cells than U87-Bev[S] cells ($P = 0.008$) (Figure 7F). These findings suggest that the mitochondria in bevacizumab-resistant xenograft cells are shifted functionally to favor glycolysis over the TCA cycle but with an associated increase in their capacity for fatty acid oxidation. This concept of triglyceride levels being higher in tissues that rely on fatty acids for fuel, which is well established in the liver, red muscle fibers, and cardiac muscle (12), is likely to be an adaptive response in bevacizumab-resistant glioblastoma cells as well.

Bevacizumab-resistant cells survive better in low glucose and GLUT3 overexpression recapitulates this phenotype. We then sought to determine if GLUT3 overexpression in resistant xenograft cells was an adaptive response to their glucose-poor microenvironment. We first confirmed that the ability of bevacizumab-resistant xenograft cells to thrive in vivo in the low tumoral glucose we identified in the microenvironments of bevacizumab-treated xenografts ($P = 0.03$; Figure 1A) was preserved in culture, with U87-Bev[R] cells exhibiting 26% greater survival after 24 hours in 0.1 g/l glucose, than U87-Bev[S] cells ($P < 0.001$; Figure 8A). We then investigated whether the glucose deprivation occurring during bevacizumab treatment drove the increased GLUT3 expression seen in resistant cells. Glucose deprivation for 24 hours increased GLUT3 mRNA
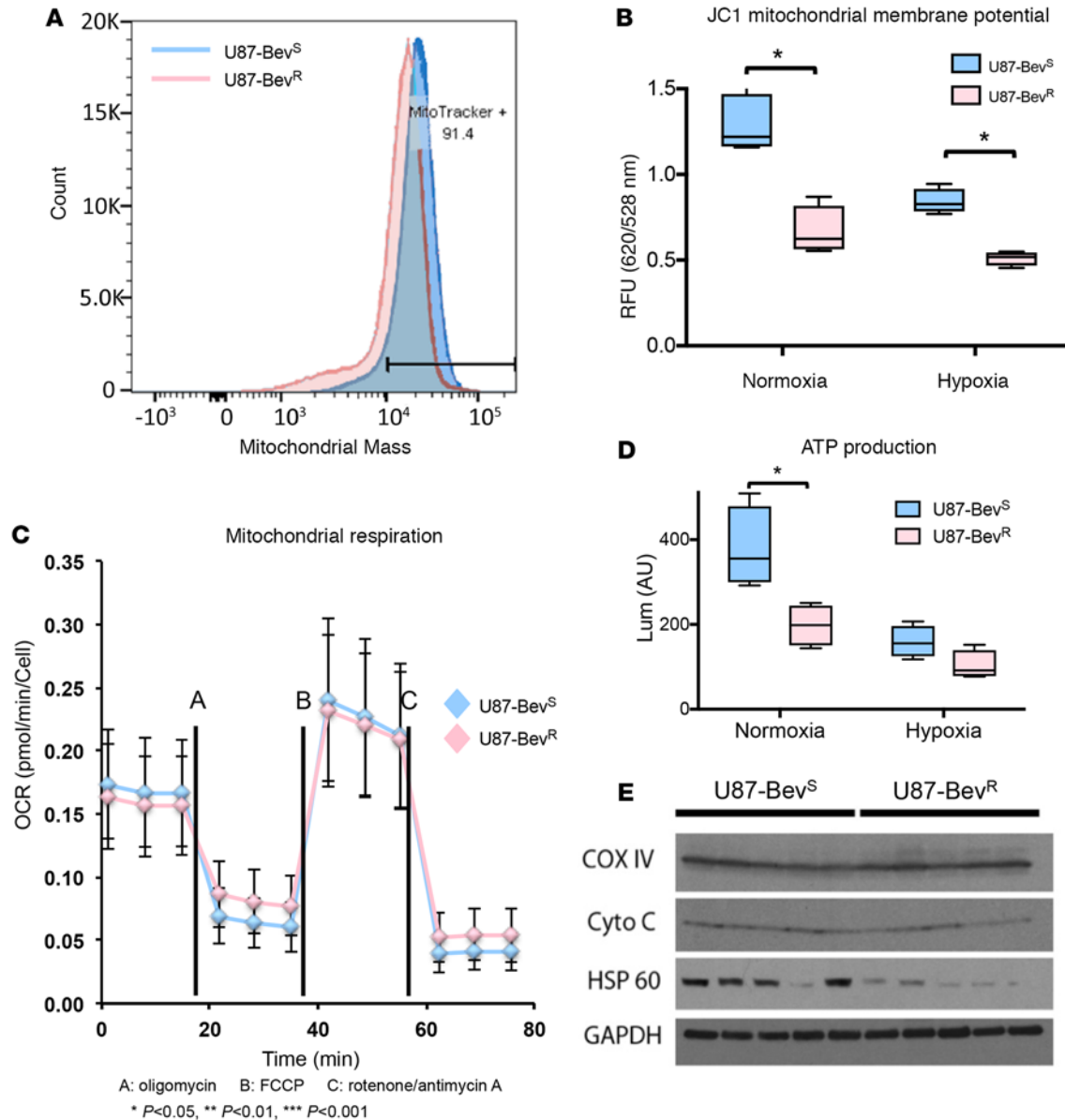
Figure 6. Decreased oxidative phosphorylation in a xenograft model of antiangiogenic therapy resistance. (**A**) Flow cytometry of bevacizumab-resistant glioma cell line–derived xenograft (U87-Bev^R) and bevacizumab-sensitive (U87-Bev^S) cells treated with MitoTracker revealed no difference in number of mitochondria per cell between the cells ($P = 0.07$, Student's t test). (**B**) Incubating cultured U87-Bev^S and U87-Bev^R cells with JC-1 fluorochrome revealed the red-to-green ratio, an indicator of mitochondrial membrane potential, to be lower in U87-Bev^R than U87-Bev^S cells in normoxia ($P = 0.03$) and hypoxia ($P = 0.03$). Furthermore, normoxic U87-Bev^R cells had a remarkably reduced membrane potential, on par with hypoxic U87-Bev^S cells ($P = 0.2$), indicating the level of mitochondrial impairment in cells from bevacizumab-resistant xenografts. Wilcoxon-Mann-Whitney test, $n = 4$/group. (**C**) Oxygen consumption rate (OCR) analysis over time when treating cells with 4 different mitochondrial inhibitors, as per the Seahorse extracellular flux analyzer protocol: oligomycin at 18 minutes, FCCP at 36 minutes, and antimycin A+rotenone at 54 minutes. U87-Bev^S had greater basal respiration before adding oligomycin ($P = 0.03$) and ATP production (basal respiration minus the proton leak between the post-oligomycin curve and the post-antimycin A+rotenone curve; $P = 0.008$) than U87-Bev^R, without a change in spare respiratory capacity (maximal respiration after adding FCCP minus basal respiration; $P = 0.8$) or proton leak ($P = 0.3$). Wilcoxon-Mann-Whitney test. For OCR curves, error bars represent SDs. (**D**) ATP production was higher in mitochondria isolated from U87-Bev^S cells and grown in 10 mM galactose and normoxia (20% oxygen), conditions selecting for oxidative phosphorylation, than mitochondria from U87-Bev^R cells ($P = 0.03$), a difference that was eliminated in hypoxia ($P = 0.1$). Wilcoxon-Mann-Whitney test, $n = 4$/group. (**E**) Western blot revealed decreased HSP60 expression in U87-Bev^R xenografts compared with U87-Bev^S xenografts ($n = 5$ tumors/group). For box-and-whisker plots, the horizontal line in the box is the median, while the box extends from the 25th to 75th percentile and the whiskers from minimum to maximum values. *$P < 0.05$.
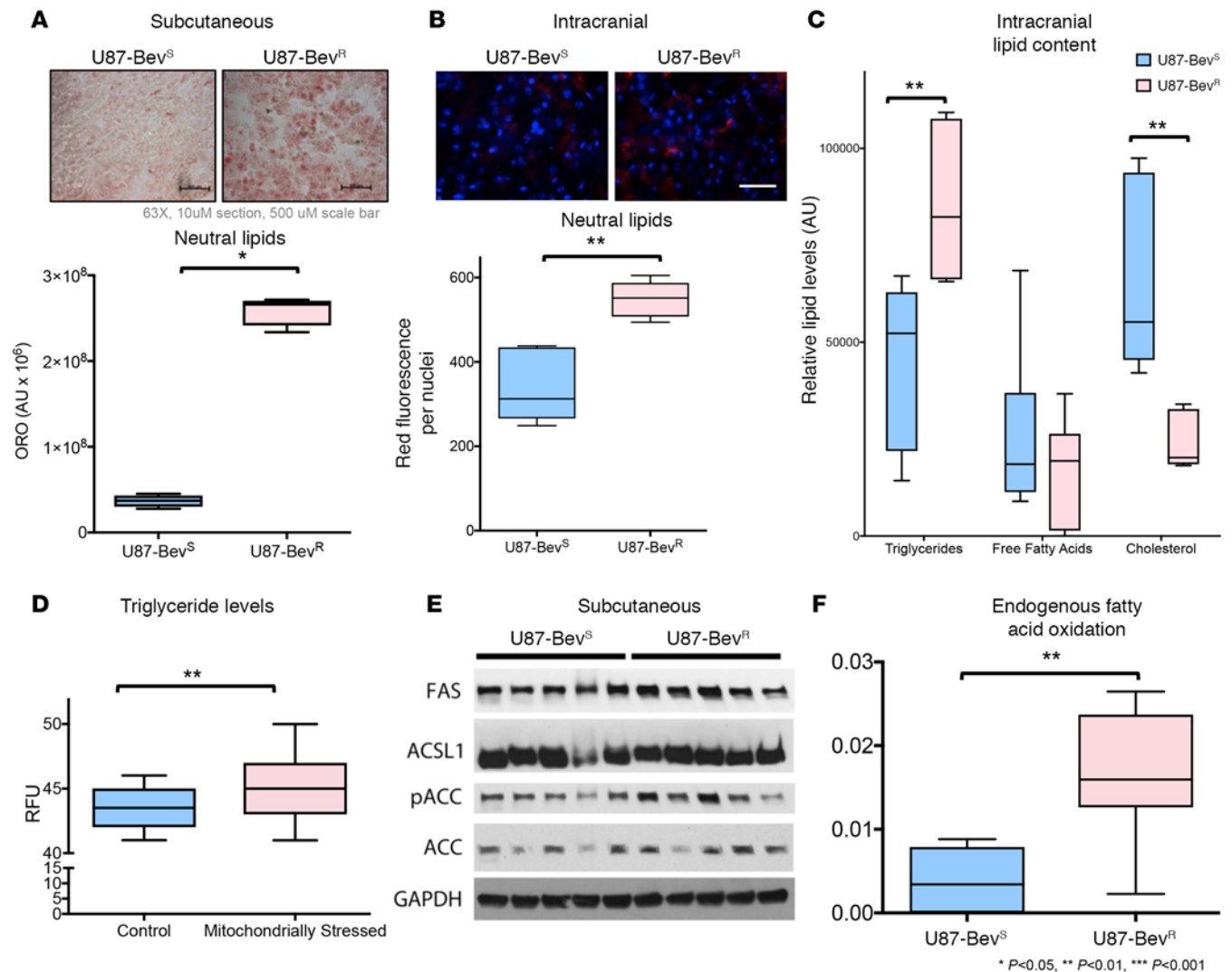
Figure 7. Changes in triglyceride levels in a xenograft model of antiangiogenic therapy resistance. (**A**) Oil Red O staining revealed increased numbers of neutral lipids in bevacizumab-resistant glioma cell line–derived (U87-Bev^R) subcutaneous xenografts compared with bevacizumab-sensitive (U87-Bev^S) subcutaneous xenografts ($P = 0.03$). Wilcoxon-Mann-Whitney test, $n = 4$/group. Magnification, ×63. Scale bars: 500 μm. (**B**) Oil Red O staining revealed increased numbers of neutral lipids in intracranial U87-Bev^R xenografts compared with intracranial U87-Bev^S xenografts ($P = 0.003$). Wilcoxon-Mann-Whitney test. Magnification, ×40. Scale bar: 750 μm. (**C**) TLC of intracranial xenografts ($n = 6$/group) revealed increased levels of triglycerides ($P = 0.009$) and decreased cholesterol ($P = 0.002$) with unchanged free fatty acids ($P = 0.4$) in U87-Bev^R xenografts compared with U87-Bev^S xenografts (Wilcoxon-Mann-Whitney test). (**D**) AdipoRed revealed increased intracellular triglyceride accumulation in U87 cells stressed with the mitochondrial inhibitors oligomycin, FCCP, antimycin A, and rotenone ($P = 0.005$). Wilcoxon-Mann-Whitney test, $n = 22$ replicates/group. (**E**) Western blot revealed no changes in triglyceride synthesis enzymes in U87-Bev^R xenografts compared with U87-Bev^S xenografts. (**F**) Oxygen consumption rate (OCR) measured to assess fatty acid oxidative metabolism using the Seahorse extracellular flux analyzer revealed that the basal respiration due to utilization of endogenous fatty acids was 18-fold higher in U87-Bev^R cells than U87-Bev^S cells ($P = 0.008$). Wilcoxon-Mann-Whitney test, $n = 6$/group. For box-and-whisker plots, the horizontal line in the box is the median, while the box extends from the 25th to 75th percentile and the whiskers from minimum to maximum values. $*P < 0.05$, $**P < 0.01$.

levels in U87-Bev^S cells ($P = 0.02$; Figure 8B) and increased GLUT3 protein levels in U87-Bev^S cells, but not as high as the baseline level of GLUT3 protein seen in U87-Bev^R cells (Figure 8C), likely reflecting the prolonged duration of bevacizumab treatment and associated glucose deprivation that U87-Bev^R cells were exposed to. We then engineered U87-Bev^S cells to overexpress GLUT3 cDNA (U87-Bev^S/GLUT3) or empty vector (U87-Bev^S/EV) (Supplemental Figure 10A) to determine whether GLUT3 overexpression recapitulated the metabolic changes seen with the resistant phenotype. We found that U87-Bev^S/GLUT3 cells exhibited 10% more glucose uptake ($P = 0.03$; Figure 8D) and nearly 3-fold more survival after 96 hours in 0.1 g/l glucose as compared with the control U87-Bev^S/EV cells ($P < 0.001$; Figure 8E). GLUT1 overexpression (Supplemental Figure 10B) did not impact cell survival in low glucose as much as GLUT3
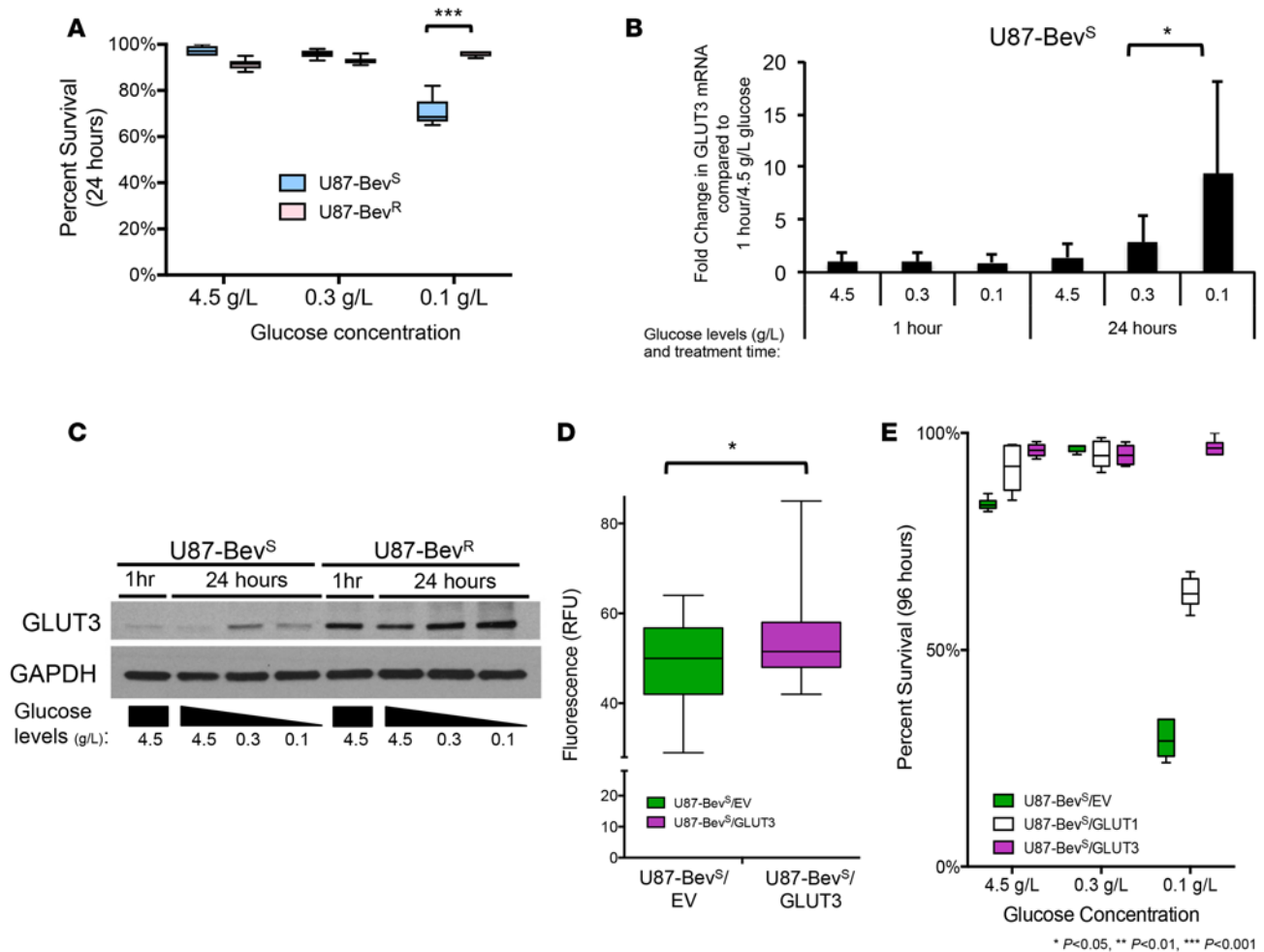
Figure 8. Bevacizumab-resistant xenograft cells exhibit greater survival in low glucose than bevacizumab-responsive cells, a phenotype replicated with GLUT3 upregulation. (**A**) Culturing bevacizumab-sensitive glioma cell line–derived xenograft (U87-Bev^S) and bevacizumab-resistant (U87-Bev^R) cells in severely low (0.1 g/l) glucose revealed greater survival of U87-Bev^R than U87-Bev^S ($P = 0.002$). Wilcoxon-Mann-Whitney test, $n = 6$/group. (**B**) Culturing of U87-Bev^S cells for 24 hours in severely low glucose levels replicating those seen with antiangiogenic therapy (0.1 g/l) increased GLUT3 transcription relative to that seen at high glucose (4.5 g/l) or moderately low glucose levels, replicating those in tumors not treated with antiangiogenic therapy (0.3 g/l). $P = 0.02$, Student's t test, $n = 3$/group. Error bars represent SDs. (**C**) Culturing of U87-Bev^S and U87-Bev^R cells in 4.5, 0.3, and 0.1 g/l glucose revealed that 24 hours in 0.1 and 0.3 g/l glucose induced GLUT3 protein expression assessed by Western blot in U87-Bev^S but still not to the levels seen in U87-Bev^R at any of the glucose concentrations. (**D**) Glucose uptake was greater in U87-Bev^S/GLUT3 cells than U87-Bev^S/empty vector (EV) cells. $P = 0.03$, Wilcoxon-Mann-Whitney test, $n = 42$/group. (**E**) U87-Bev^S/GLUT3, U87-Bev^S/GLUT1, and U87-Bev^S/EV cell survival in 4.5, 0.3, and 0.1 g/l glucose after 96 hours was affected by both the glucose concentration ($P < 0.0001$) and the nature of the overexpressed glucose transporter, with GLUT3 promoting more survival than GLUT1 ($P < 0.0001$), and interaction occurring between these variables. $P < 0.0001$, ANOVA, $n = 6$/group. For box-and-whisker plots, the horizontal line in the box is the median, while the box extends from the 25th to 75th percentile and the whiskers from minimum to maximum values. *$P < 0.05$, ***$P < 0.001$.

overexpression (Figure 8E). Cell cycle analysis revealed that, after 48 hours, decreasing glucose caused cells to accumulate in the G1/G0 phase and out of S phase ($P < 0.0001$), while GLUT3 overexpression allowed escape out of G1/G0 phase ($P = 0.0001$) and into S phase ($P = 0.003$), with no interaction between these 2 variables ($P = 0.4$; ANOVA) (Supplemental Figure 11). These findings suggest that GLUT3 overexpression allowed cells to overcome the G1/S checkpoint in low glucose. Thus, GLUT3 overexpression recapitulated the glucose uptake and survival and proliferation in a low glucose environment that we noted in cells from bevacizumab-resistant xenografts, revealing its crucial role in the resistant phenotype.

GLUT3 overexpression endows tumor cells with the same metabolic phenotype as bevacizumab-resistant cells. We then investigated the metabolic effects of GLUT3 overexpression in U87-Bev^S glioblastoma cells. U87-Bev^S/GLUT3 cells exhibited increased glycolysis compared with U87-Bev^S/EV cells based on extracellular acidification assessed by a Seahorse extracellular flux analyzer (range: $P < 0.001$ to $P = 0.02$); Figure 9A). U87-Bev^S/GLUT3 cells also exhibited decreased basal mitochondrial respiration ($P < 0.0001$) and ATP production ($P < 0.0001$), with no change in proton leak ($P = 0.2$) or spare respiratory
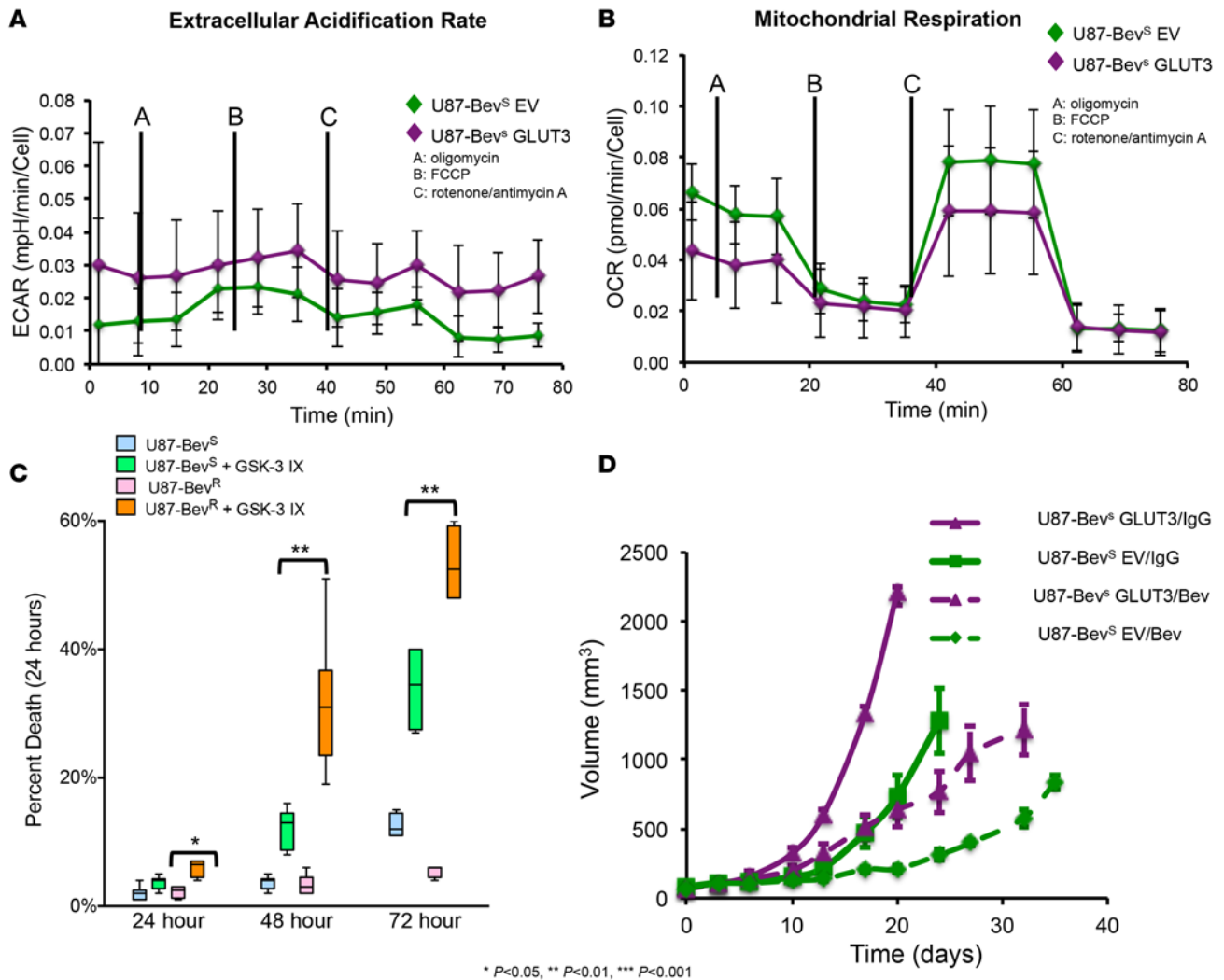
Figure 9. GLUT3 upregulation drives the metabolic and therapeutic response changes associated with resistance to antiangiogenic therapy in a targetable manner. (**A**) Extracellular acidification rate (ECAR) over time, a marker of glycolysis, was higher in cultured bevacizumab-sensitive glioma cell line–derived xenograft cells transfected with GLUT3 (U87-Bev[S]/GLUT3) cells vs. U87-Bev[S]/empty vector (EV) cells treated with various oxidative phosphorylation inhibitors (range: $P < 0.0001$–0.02). Wilcoxon-Mann-Whitney test, $n = 46$/group. (**B**) Oxygen consumption rate (OCR) over time after treatment with 4 different mitochondrial inhibitors, as per the Seahorse extracellular flux analyzer protocol: oligomycin at 18 minutes, FCCP at 36 minutes, and antimycin A+rotenone at 54 minutes. Basal respiration (rate prior to oligomycin injection minus nonmitochondrial respiration) and ATP production (basal respiration minus proton leak) were higher in U87-Bev[S]/EV than U87-Bev[S]/GLUT3. $P < 0.0001$, Wilcoxon-Mann-Whitney test, $n = 46$/group. For ECAR and OCR curves in **A** and **B**, error bars represent SDs. (**C**) Glycogen synthase kinase-3β inhibitor GSK-3 IX (10 μM) caused more cell death in bevacizumab-resistant (U87-Bev[R]) cells than U87-Bev[S] cells after 24 ($P = 0.04$), 48 ($P = 0.005$), and 72 ($P = 0.006$) hours. Student's t test, $n = 6$/group. For box-and-whisker plots, the horizontal line in the box is the median, while the box extends from the 25th to 75th percentile and the whiskers from minimum to maximum values. *$P < 0.05$, **$P < 0.01$. (**D**) Subcutaneous xenografts derived from U87-Bev[S]/GLUT3 and U87-Bev[S]/EV cells were treated with bevacizumab or control IgG antibody ($n = 6$/group). After 20 days, GLUT3 overexpression promoted tumor growth in vivo ($P = 0.006$) while bevacizumab reduced tumor growth ($P < 0.0001$), with no interaction between these variables ($P = 0.1$, ANOVA). For tumor volumes, values and error bars represent mean ± SEM.

capacity ($P = 0.5$) compared with U87-Bev[S]/EV cells (Figure 9B and Supplemental Figure 12), the same features of oxidative phosphorylation noted in bevacizumab-resistant cells (Figure 2C and Supplemental Figure 5). In contrast, GLUT3 expression did not drive the invasion described by our group (3, 9, 13) and others (6) in bevacizumab-resistant cells, as U87-Bev[S]/GLUT3 and U87-Bev[S]/EV cells were equally invasive in scratch assays ($P = 0.8$–0.9; Supplemental Figure 13). Thus, GLUT3 expression was specifically associated with the crucial changes in glycolysis and oxidative phosphorylation, which we noted to be the hallmarks of bevacizumab-resistant cells.

GLUT3 overexpression is a targetable mediator in bevacizumab-resistant tumor cells sufficient to endow the rapid growth and ineffective bevacizumab response seen in resistant tumors. While specific inhibitors of GLUT3 have

yet to be developed, glycogen synthase kinase-3β (GSK-3β) inhibitors have been shown to target GLUT3-overexpressing cells by downregulating GLUT3 transcription (14). We therefore investigated the impact of the GSK-3β inhibitor GSK-3 IX (14) on the survival of U87-Bev^R versus U87-Bev^S cells in 0.3 g/l glucose and found that 10 μM GSK-3 IX caused more cell death in U87-Bev^R cells than U87-Bev^S cells after 24 ($P = 0.04$), 48 ($P = 0.005$), and 72 ($P = 0.006$) hours (Figure 9C) and downregulated GLUT3 transcription in these cells ($P = 0.0004–0.02$) (Supplemental Figure 14). We then treated subcutaneous xenografts derived from U87-Bev^S/GLUT3 and U87-Bev^S/EV cells with bevacizumab or control IgG antibody. After 20 days, GLUT3 overexpression promoted tumor growth in vivo ($P = 0.006$) while bevacizumab reduced tumor growth ($P < 0.0001$), with no interaction between these variables ($P = 0.1$; ANOVA; Figure 9D). Indeed, U87-Bev^S/GLUT3 xenografts grew so fast that, while there was technically a statistically significant response to bevacizumab treatment relative to IgG treatment, bevacizumab treatment only reduced the growth rate of U87-Bev^S/GLUT3 xenografts to that of IgG-treated U87-Bev^S/EV xenografts (Figure 9D). Ki-67 labeling revealed that bevacizumab treatment lowered ($P = 0.002$) and GLUT3 overexpression raised ($P = 0.01$) Ki-67 labeling, with no interaction between these 2 variables ($P = 0.2$; ANOVA) (Supplemental Figure 15). This acceleration of growth in the face of treatment is the change in phenotype associated with clinical resistance, a definition often made without an associated control-treated group.

Discussion

The initial optimism that greeted the introduction of antiangiogenic therapies like bevacizumab into the clinic has been tempered by the realization that these agents typically have transient responses. Studies of tumors that evolve to be become resistant to these treatments performed by our group and others have revealed these tumors to be hypoxic and, in one study, exhibit low glucose (7). Thus, resistance to antiangiogenic therapy evolves despite the treatment accomplishing its goals of cutting off oxygen and nutrient supply to the tumor. Indeed, our HIF-1α analysis suggests that the sensitive tumors respond to bevacizumab with maintenance of oxygenation but the resistant xenografts respond to bevacizumab with worsening hypoxia, consistent with other studies suggesting that these therapies cause a vascular normalization window beyond which their effects start to become more adverse (15).

We have previously reported hypoxia-induced autophagy as a mechanism by which tumors resistant to antiangiogenic therapy survive the hypoxia induced by these treatments (5). However, these resistant tumors do more than just survive hypoxia; they thrive in the harsh oxygen- and nutrient-poor microenvironment resulting from the devascularization caused by antiangiogenic therapy. Understanding the metabolic reprogramming that defines this resistance requires the ability to analyze fresh resistant tumors. We overcame this critical barrier using our 2 potentially novel xenograft models of bevacizumab resistance. While the U87 cell line has evolved changes from the time of its initial creation that may impact its utility as a brain tumor model (16), the ability to compare isogeneic cells differing only in bevacizumab responsiveness in U87-Bev^R versus U87-Bev^S is valuable, and the use of a second patient-derived set of xenografts reduces concerns that our findings are affected by the use of U87 cells and ensures broader applicability of our findings to glioblastoma.

These models yielded important distinct findings compared with previous studies, such as our finding of unchanged number of mitochondria in resistant versus sensitive xenografts, a finding that contrasts with reports of decreased mitochondria in bevacizumab-treated xenografts (17, 18). These findings suggest that a recovery of mitochondrial mass lost during initial treatment occurs during the evolution of resistance to antiangiogenic therapy despite persistent functional impairment of these mitochondria.

Analysis of our xenograft models revealed resistance to be defined by an expansion of the Warburg effect in which the cancer cells become more reliant on glycolysis and even less dependent on oxidative phosphorylation than cancer cells normally are. Increased reliance on the Warburg effect would certainly enable these tumor cells to thrive in hypoxia and the glucose-poor microenvironment induced by antiangiogenic therapy. We added to this finding with the potentially novel demonstration that resistant cells go beyond expanding their reliance on the Warburg effect by becoming more efficient at glucose uptake through increased expression of GLUT3, which we demonstrated in 2 xenograft models of bevacizumab resistance and paired glioblastomas before and after bevacizumab resistance. We also found that GLUT3 overexpression drove more than just the glucose uptake associated with bevacizumab resistance, as it promoted the increased glycolysis, impaired oxidative phosphorylation, and proliferation in low glucose associated with bevacizumab resistance. Furthermore, the stress of inhibited oxidative phosphorylation

caused by GLUT3 overexpression could be the source of the increased triglycerides we found in resistant xenografts. Indeed, a link between GLUT3 expression and intracellular triglycerides has been described in macrophages (19). Thus, GLUT3 upregulation promotes the metabolic engine that defines resistance to antiangiogenic therapy.

GLUT3 is most specifically expressed in neurons and has both a higher affinity for glucose and at least a 5-fold greater transport capacity than GLUT1, GLUT2, and GLUT4. This higher affinity for glucose is particularly significant for the role of GLUT3 in neuronal glucose transport, because ambient glucose levels surrounding the neurons are 5-fold lower than in serum (20, 21). While cancer cells express all 4 of these GLUTs, GLUT3 may be the predominant one in cancers such as glioblastoma (22), where it has been associated with aggressive aspects of cancer such as the epithelial to mesenchymal transition (23) and the tumor-initiating stem cells of glioblastoma (24). Interestingly, GLUT3 overexpression has also been described in temozolomide-resistant glioblastoma cell lines established in culture (25). Further work will also be needed to define whether the glycosylated versus nonglycosylated forms of GLUT3, both of which were detected in our study, serve different functional roles in the context of resistance to antiangiogenic therapy, as has been suggested for GLUT1 for some tumor cells in the absence of therapeutic stressors (26).

Specific pharmacologic inhibitors of GLUT3 are not available at present but will be important to develop as cancer treatments, including in conjunction with antiangiogenic therapy. For now, based on a study showing that some inhibitors of the serine/threonine kinase GSK-3β downregulate GLUT3 expression (14), we demonstrated that the GSK-3β inhibitor GSK-3 IX lowered GLUT3 transcription and caused preferential toxicity in our bevacizumab-resistant xenograft cells, suggesting a potential targetable metabolic vulnerability of bevacizumab-resistant glioblastomas. Further study will be needed to determine if GSK-3 IX penetrates the blood-brain barrier and can be used to treat intracranial tumors, or to identify a GSK-3β inhibitor that downregulates GLUT3 expression and crosses the blood-brain barrier. Targeting the increased dependence on glycolysis in bevacizumab-resistant tumors cells could also be accomplished using any of the recently developed glycolysis inhibitors, several of which have undergone clinical trials (27, 28). The therapeutic selectivity of these agents for cancer cells would likely be further augmented in the setting of resistance to antiangiogenic therapy given the upregulation of the Warburg effect we noted in these resistant tumors.

Of note, we previously showed that patient glioblastomas resistant to bevacizumab exhibit increased proliferation or invasion in a manner that correlated with imaging features (3), with subsequent studies from our group implicating c-Met and β1 integrin in the increased invasiveness (8, 9). Our findings here suggest that GLUT3 upregulation contributes to the increased proliferation, but not the increased invasiveness, seen in these bevacizumab-resistant tumors. While this proliferation alone was not enough to render GLUT3-overexpressing xenografts resistant to bevacizumab, it was enough to render their volumetric growth curve after treatment with bevacizumab an exponential one resembling that of an untreated tumor without GLUT3 overexpression. Further work will be needed to determine if the combination of GLUT3 overexpression and increased expression of invasion mediators is needed to drive a xenograft to completely fail to respond to bevacizumab. Site-directed biopsies such as those used in this study could also be used to determine if patient bevacizumab-resistant glioblastomas enrich proliferation-driving GLUT3 versus invasion-driving c-Met and β1 integrin in different regions of resistant tumors. Importantly, just as our previous work revealed increased c-Met and β1 integrin to be targetable vulnerabilities during bevacizumab resistance (8, 9), our study of GSK-3 IX revealed increased GLUT3 expression to also be a potentially targetable vulnerability in these tumors.

In conclusion, we identified comprehensive metabolic reprogramming in tumors resistant to antiangiogenic therapy emanating from increased expression of the GLUT3 isoform of the glucose transporter. Future studies should investigate whether the mitochondrial impairment and increased reliance on glycolysis we noted in resistant tumors represents an exploitable weakness, the targeting of which would enable antiangiogenic therapy to fulfill its tremendous therapeutic promise.

Methods

General cell culture. U87 glioma cells (ATCC), U87-Bev^R cells (freshly harvested from xenografts as described below), and U87-Bev^S cells (freshly harvested from xenografts as described below) were cultured in DMEM/F-12 (1:1) mixture media containing high (4.5 g/l), intermediate (0.3 g/l), and low (0.1 g/l) glucose concentrations supplemented with 10% FBS and 1% penicillin/streptomycin and maintained in

a standard 37°C incubator. For comparisons of hypoxia versus normoxia, cells were cultured in either normoxic (5% CO_2, 21% O_2, 74% N_2) or hypoxic conditions (5% CO_2, 1% O_2, 94% N_2) in a humidified O_2-controlled incubator (Sanyo) at 37°C that contained only the cells being studied and was never opened for the duration of incubation. For some experiments, cells were treated with GSK-3 IX (Santa Cruz Biotechnology) at 10 μM for 24, 48, or 72 hours or YC-1 (AG Scientific) at 10 μM for 0, 6, 12, or 24 hours, with both drugs suspended in DMSO as a stock solution before diluting into media.

Plasmids and transduction/transfection. The lentiviral GLUT3 cDNA expression vector was constructed by cloning a human SLC2A3 sequence-verified cDNA insert (GE Dharmacon, MHS6278-202757852) into the pLenti6.3/V5-DEST Gateway vector (Invitrogen, V533-06) using a pENTR/D-TOPO Cloning Kit (Thermo Fisher Scientific, K2400-20). Lentiviral particles were generated using ViraPower Lentiviral Packaging Mix (Thermo Fisher Scientific, K4975-00). U87-Bev^S cells were transduced with lentivirus expressing GLUT3 or empty vector (EV) in high-glucose DMEM containing 6 μg/ml Polybrene (Santa Cruz Biotechnology, sc-134220). U87-Bev^S cells were transfected with pcDNA3.2/v5-DEST hGlut1 (Addgene, plasmid 18085) using Fugene 6 (Promega, E2691). DNA/lipid compound ratio and incubation time were selected according to the manufacturer's recommendations. Optimem Medium (UCSF Cell Culture Facility, 31985070) was used as transfection medium. Transfected cells were selected with G418 Sulfate (Thermo Fisher Scientific, 11811023).

Site-directed biopsies. Biopsies were performed utilizing a three-dimensional intraoperative navigation system. Fresh regional biopsy tissues were dissociated using the gentleMACS dissociator and the human tumor dissociation kit (Mitenyi Biotec).

qPCR. Total cellular RNA was isolated with a RNeasy kit (Qiagen) and reverse transcribed into cDNA with Superscript III (Invitrogen). Power Syber Green Master Mix (Applied Biosystems) was used with the following primers: *GLUT3* (human) forward 5′-CGTTGTTGGAATTCTGGTGGC-3′ and reverse 5′-CTTAGCATTCTCCTCTTCTTTT-3′; *HSP60* (human) forward 5′-TGGTGACAATAGAAAGAAC-CAGCTT-3′ and reverse 5′-GTCAATCCCTCTTCTCCAAACACT-3′; *GAPDH* (human) forward 5′-GCT-GAGAACGGGAAGCTTGT-3′ and reverse 5′-TCTCCATGGTGGTGAAGACG-3′; and *ACTB* (human) forward 5′-GGCATCCTCACCCTGAAGTA-3′ and reverse 5′-GGGGTGTTGAAGGTCTCAAA-3′. qPCR was performed on an Applied Biosystems 7900 HT cycler. For relative quantification, to determine measured gene expression variation between treated samples and controls, cDNA obtained as described above was diluted to a constant concentration for all samples. Samples were prepared in triplicate for each primer pair of interest, using PCR setup conditions described by Power Syber Green Protocol (Thermo Fisher Scientific). All samples were run in triplicate using GAPDH qPCR primers as a relative quantification standard. Results obtained from this experiment were normalized to both GAPDH and sample control using the $2^{-\Delta\Delta Ct}$ method. For absolute quantification of gene mRNA copy number, a standard curve was constructed by plotting Ct values against logarithmic concentrations of a serially diluted *ACTB* plasmid, with dilutions ranging between 10^6 and 10^1 copies per reaction. Samples of interest were prepared as described for the relative quantification, with *ACTB* qPCR primers used as an endogenous control for sample loading and variable cDNA concentrations. Results were adjusted to said control by normalizing the relative abundance of ACTB to that of the target gene, allowing normalized target gene values to be directly compared (29). The exact copy numbers of target genes in normalized samples were quantified by interpolating Ct values against the standard curve.

Mitochondrial isolation. Mitochondria were isolated from cells using a Mitochondria Isolation Kit for Cultured Cells (Thermo Fisher Scientific, 89874), per the manufacturer's protocol.

Western blot analysis. For immunoblotting assays, human xenograft lysates and cellular preparations were harvested in radioimmunoprecipitation assay buffer (RIPA) containing 20 mM Tris-HCl (pH 7.5), 150 mM NaCl, 1 mM Na_2EDTA, 1% NP-40, 1% sodium deoxycholate, 2.5 mM sodium pyrophosphate, 1 mM β-glycerophosphate, 1 mM Na_3VO_4, 1 μg/ml leupeptin (RIPA Buffer, 10×, Cell Signaling Technology, catalog 9806) and 1 tablet each of PhoStop and Complete Mini (Roche). Removal of insoluble materials was achieved by centrifugation at 20,160 *g* for 20 minutes at 4°C. Protein concentration was then determined using the bicinchoninic acid (BCA) assay (Pierce Biotechnology). Samples were then prepared to contain 10–30 μg total protein in RIPA buffer with 4× NuPAGE LDS loading buffer (Life Technologies, catalog LP0001). These samples were electrophoresed in an SDS-PAGE gel, transferred to a PVDF membrane, and then probed with antibodies against hexokinase I (1:1,000; catalog 2024P), hexokinase II (1:1,000; catalog 2867P), phosphofructokinase (1:1,000; catalog 8164P), pyruvate kinase-M2 (1:1,000; catalog 4053P),

lactate dehydrogenase A (1:1,000; catalog 3582P), pyruvate dehydrogenase (1:1,000; catalog 3205P), COX IV (1:1,000; catalog 4850P), cytochrome C (1:1,000; catalog 4280S), HSP60 (1:1,000; catalog 4869S), fatty acid synthase (1:1,000; catalog 3180S), ACSL1 (1:1,000; catalog 9189P), phospho-acetyl-CoA carboxylase (1:1,000; catalog 3661), acetyl-CoA carboxylase (1:1,000; catalog 3676) (all Cell Signalling Technology); GLUT1 (1:500, catalog 07-1401), GAPDH (1:50,000; catalog mab374) (both Millipore); GLUT3 (1:400, catalog ab15311 or ab53095), hexokinase III (1:500, catalog ab126217), pyruvate dehydrogenase kinase isoform 2 (1:1,000; catalog ab76152), and HIF-1α (1:200, catalog ab1) (all Abcam). The resulting membranes were then detected using HRP-conjugated secondary antibodies against mouse (catalog 7076S), or rabbit (catalog 7074S) (both Cell Signaling Technology) at a dilution of 1:2,000 for 1 hour at room temperature and developed using Clarity Western ECL substrate (Bio-Rad Laboratories, catalog 10026385 Rev A) and radiographic film.

Colorimetric assays. Mitochondria isolated from a kit per manufacturer's protocol (Thermo Fisher Scientific, 89874) and whole cells were analyzed for intracellular ATP using the ATPlite Luminescence Assay System (PerkinElmer, 6019641) per the manufacturer's protocol. Glucose levels were measured in tumor tissues after lysing the tissue with a dounce homogenizer, deproteinating the tissue and measuring absorbance using a Glucose Colorimetric Assay Kit (Cayman Chemical, 100009582). Pyruvate concentrations, mitochondrial membrane potential, glucose uptake, and glycolysis rates were measured using a Pyruvate Assay Kit (Cayman Chemical, 700470), JC-1 Mitochondrial Membrane Potential Kit (Cayman Chemical, 10009172), Glucose Uptake Cell-Based Assay Kit (Cayman Chemical, 600470), Glucose Assay Kit used for tissue (Cell Biolabs Inc., STA-681), and Glycolysis Cell-Based Assay Kit (Cayman Chemical, 600450), respectively. ATP levels were measured using ATPlite Luminescence Assay System. Fluorescence was measured using a BioTek Synergy 2 plate reader. To analyze mitochondrial mass, 1×10^6 cells were washed with PBS, trypsinized in 0.25% trypsin with EDTA, counted, and incubated with 100 nM MitoTracker Deep Red FM (Thermo Fisher Scientific, M22426), and fixed with 4% paraformaldehyde. Flow cytometry was conducted on a BD FACS Aria 3 and analyzed using FlowJo software (Tree Star, Inc).

Cell cycle analysis. U87 empty vector– and GLUT3 cDNA–transfected cells were plated on 6-cm dishes with DMEM containing 4.5 g/l glucose, 10% FBS, and 1% penicillin/streptomycin and incubated at 37°C for 24 hours. Dishes were then washed twice with Dulbecco's PBS (DPBS), serum starved for 12 hours, and then swapped with complete DMEM containing 0.1, 0.3, and 4.5 g/l glucose. At 24 and 48 hours, cells were harvested with trypsin, pelleted, and washed twice with DPBS. After aspirating supernatant, 5 ml of 4°C 70% ethanol was added dropwise while vortexing. The mixtures were incubated on ice for 30 minutes, then washed with deionized H_2O followed by DPBS. The pellet was then resuspended at 1×10^6 cells/ml in DPBS with 0.1 mg/ml RNase A (Life Technologies, EN0531) and incubated for 15 minutes at 37°C. Propidium iodide (Anaspec, AS-83215) was added to a final concentration of 50 μg/ml and cells were then analyzed by flow cytometry (Sony SH800).

Animal studies. The establishment of our subcutaneous and intracranial bevacizumab-resistant U87-Bev[R] and bevacizumab-responsive U87-Bev[S] xenografts and patient-derived bevacizumab-resistant SF7796 and bevacizumab-responsive GBM43 and SF7300 xenografts has been previously described (8, 10). Subcutaneous and intracranial xenografts were derived from U87-Bev[S]/GLUT3 and U87 U87-Bev[S]/EV cells by injecting 5×10^5 cells subcutaneously into the flank and 10^5 cells stereotactically into the right caudate (orthotopic model) of 3- to 4-week-old female athymic mice (Simonson Laboratories). At the study endpoint we performed cardiac perfusion in tumor-bearing mice following a lethal dose of 2.5% Avertin in PBS, followed by 1% paraformaldehyde in PBS. Tumors were removed and preserved in optimal cutting temperature (OCT) medium (Sakura Finetek) at –80°C. Sections were then cut at 10 μm on a Leica CM1950 cryostat and dried at 37°C overnight. To measure intratumoral glucose, one piece of tumor was weighed, fractionated with a scalpel, and dissociated using RPMI supplemented with DNase I (Worthington Biochemical, LS006342) and Collagenase IV (Worthington Biochemical, LS004186). This solution was then washed twice with FACS buffer (HBSS with 2% added FBS), then RBCs were lysed using RBC lysis buffer. Remaining cells were washed once more in FACS buffer and then resuspended in 10 ml FACS buffer for counting. Cell counts were obtained in duplicate and averaged using an Invitrogen Countess machine and slides. In doing so, the cells per weight of tumor were derived. In parallel, the Cell Biolabs Glucose Assay Kit was used on a tumor lysate from a second piece of tumor, from which μmol glucose per tumor weight was derived. From the 2 values (cells/weight tumor and μmol glucose/tumor weight), μmol glucose per million cells was calculated.

Immunohistochemistry. Frozen tissue sections were washed twice with PBS before fixation with –20°C acetone for 10 minutes at room temperature, then the acetone was allowed to evaporate for 20 minutes. For peroxidase-based staining, slides were then washed once with PBS before blocking endogenous peroxidase with 0.3% H_2O_2 in PBS for 10 minutes. Slides were then washed 3 times with PBS, 1 time with PBS + 1% Triton X-100 (Sigma-Aldrich, X100), followed by 3 washes with PBS. Tissue sections were blocked with TNB (PerkinElmer, FP1020) for 30 minutes and then incubated with antibodies against Ki-67 (goat polyclonal, 1:100, Santa Cruz Biotechnology, catalog sc-7846), HIF-1α (mouse monoclonal, 1:250, Abcam, catalog ab1), or GLUT3 (rabbit polyclonal, 1:250, Abcam, catalog ab53095) in TNB overnight at 4°C. Slides were washed as described above, after which slides were incubated with the appropriate secondary (1:100 bovine anti-goat IgG-HRP, Santa Cruz Biotechnology, catalog sc-2384; 1:250 Alexa-Fluor 488 donkey anti–mouse IgG, Invitrogen, catalog A21202; or 1:250 Alexa-Fluor 555 Fab goat anti–rabbit IgG, Life Technologies, catalog A21430) for 1 hour at room temperature, followed by 3 washes with PBS. For peroxidase staining, tissue sections were developed with a DAB kit (Vector Laboratories Inc., SK-4100) followed by counterstaining with hematoxylin and mounting of coverslips with Cytoseal 60 (Thermo Fisher Scientific, 83104), while for fluorescent stains, tissue sections were coverslipped with DAPI Fluoromount (Southernbiotech, 0100-20). Images were captured with a 40× objective on a Zeiss AxioImager M1 and analyzed by ImageJ (NIH).

Seahorse extracellular flux analyzer. Oxygen consumption rates (OCRs) and extracellular acidification rates (ECARs) were determined using an XF96 Extracellular Flux Analyzer (Seahorse Bioscience; a gift from the S.D. Bechtel Junior Foundation in San Francisco, California, USA to the Gladstone Institutes). Cell density and drug concentrations were optimized to 10,000 cells/well and 1 μM oligomycin and 1 μM FCCP. Briefly, cells were plated in high-glucose DMEM and incubated overnight. The following day, the adherent cells were washed and fresh XF Cell Mito Stress Test Assay medium was added (Seahorse XF Base media supplemented with 2.5 mM glucose, 2 mM glutamine, and 1 mM sodium pyruvate). Mito Stress Test metabolic inhibitors were added sequentially: 1 μM oligomycin, 1 μM FCCP, 1 μM rotenone, and 1 μM antimycin A. Basal OCRs and ECARs were measured and compared with drug-induced changes in OCR and ECAR. Parameters were calculated per the manufacturer's protocol. Measurements were normalized to cell count using Cyquant (Life Technologies, C7026).

^{13}C NMR. ^{13}C NMR of cultured cells was performed as previously described (30).

Lipid staining. Lipid staining was performed with Oil Red O (Santa Cruz Biotechnolgy, sc-203749) peroxidase- or fluorescence-based staining and analyzed as previously described (31). Intracellular triglyceride accumulation was measured using AdipoRed (Lonza, PT-7009), with 485/572 nm excitation/emission measured using the BioTek/Synergy 2 plate reader.

TLC. Lipid content was analyzed with TLC, as described by Koliwad et al. (32). Briefly, tissue was homogenized in cold Tris-sucrose buffer, extracted with chloroform/methanol (2:1), and separated with hexane/ethyl ether/acetic acid (80:20:1) on silica gel plates. Samples were normalized to protein concentration using a BCA assay (Pierce), and densitometry was quantified using ImageJ.

Statistics. For comparing continuous variables, a Shapiro-Wilk test was used to determine whether there was a normal distribution. If analyzed variables exhibited a normal distribution, a Student's *t* test (paired if the variables were paired, unpaired if they were not paired) was used to compare the variables. If analyzed variables exhibited a non-normal distribution, nonparametric tests were used to compare the variables. If the non-normally distributed groups were not paired, the comparison was rendered with a Wilcoxon-Mann-Whitney test. If non-normally distributed groups were paired, the comparison was rendered with a Wilcoxon signed-rank test. To render multiple comparisons of normally distributed variables when there was homogeneity of variances, 2-way ANOVA was used to analyze for main effects and interactions. Because non-normally distributed variables could not be analyzed for interaction, multiple comparisons of non-normally distributed variables were rendered through multiple Wilcoxon-Mann-Whitney tests performed on each group of 2 samples in the data. *P* values are 2-tailed and values below 0.05 were considered statistically significant.

Study approval. All mice studies were approved as being in compliance with institutional ethical regulations by the UCSF IACUC (approval number AN105170-02). Site-directed biopsies of patient glioblastomas were performed with informed consent and IRB approval (number 11-06160).

Author contributions

MKA conceptualized the study. RK, SM, AJ, AN, AC, PMF, GY, JRW, MD, DC, BAC, JH, MS, JLIG, and PE developed the methodology. SR, SK, and MKA conducted the investigation. MKA wrote

the original draft of the manuscript. RK, SM, AJ, AN, AC, PMF, SK, MKA, AM, and JP reviewed and edited the manuscript. MKA acquired funding. SR, SK, and MKA provided equipment. SR, SK, and MKA supervised the study.

Corresponding author: Manish K. Aghi, MD, PhD; Professor of Neurological Surgery; University of California at San Francisco (UCSF); 505 Parnassus Avenue Room M779; San Francisco, California 94143-0112, USA. Phone: 415.353.1172; E-mail: manish.aghi@ucsf.edu.

1. Bergers G, Hanahan D. Modes of resistance to anti-angiogenic therapy. *Nat Rev Cancer*. 2008;8(8):592–603.
2. Kreisl TN, et al. Phase II trial of single-agent bevacizumab followed by bevacizumab plus irinotecan at tumor progression in recurrent glioblastoma. *J Clin Oncol*. 2009;27(5):740–745.
3. DeLay M, et al. Microarray analysis verifies two distinct phenotypes of glioblastomas resistant to antiangiogenic therapy. *Clin Cancer Res*. 2012;18(10):2930–2942.
4. Clark AJ, et al. Neurosurgical management and prognosis of patients with glioblastoma that progresses during bevacizumab treatment. *Neurosurgery*. 2012;70(2):361–370.
5. Hu YL, et al. Hypoxia-induced autophagy promotes tumor cell survival and adaptation to antiangiogenic treatment in glioblastoma. *Cancer Res*. 2012;72(7):1773–1783.
6. Pàez-Ribes M, et al. Antiangiogenic therapy elicits malignant progression of tumors to increased local invasion and distant metastasis. *Cancer Cell*. 2009;15(3):220–231.
7. Nardo G, et al. Glycolytic phenotype and AMP kinase modify the pathologic response of tumor xenografts to VEGF neutralization. *Cancer Res*. 2011;71(12):4214–4225.
8. Carbonell WS, DeLay M, Jahangiri A, Park CC, Aghi MK. β1 integrin targeting potentiates antiangiogenic therapy and inhibits the growth of bevacizumab-resistant glioblastoma. *Cancer Res*. 2013;73(10):3145–3154.
9. Jahangiri A, et al. Gene expression profile identifies tyrosine kinase c-Met as a targetable mediator of antiangiogenic therapy resistance. *Clin Cancer Res*. 2013;19(7):1773–1783.
10. Jahangiri A, et al. Gene expression profile identifies tyrosine kinase c-Met as a targetable mediator of antiangiogenic therapy resistance. *Clin Cancer Res*. 2013;19(7):1773–1783.
11. Veereshwarayya V, Kumar P, Rosen KM, Mestril R, Querfurth HW. Differential effects of mitochondrial heat shock protein 60 and related molecular chaperones to prevent intracellular beta-amyloid-induced inhibition of complex IV and limit apoptosis. *J Biol Chem*. 2006;281(40):29468–29478.
12. Frayn KN, Arner P, Yki-Järvinen H. Fatty acid metabolism in adipose tissue, muscle and liver in health and disease. *Essays Biochem*. 2006;42:89–103.
13. Carbonell WS, Murase S, Horwitz AF, Mandell JW. Migration of perilesional microglia after focal brain injury and modulation by CC chemokine receptor 5: an in situ time-lapse confocal imaging study. *J Neurosci*. 2005;25(30):7040–7047.
14. Watanabe M, Abe N, Oshikiri Y, Stanbridge EJ, Kitagawa T. Selective growth inhibition by glycogen synthase kinase-3 inhibitors in tumorigenic HeLa hybrid cells is mediated through NF-κB-dependent GLUT3 expression. *Oncogenesis*. 2012;1:e21.
15. Winkler F, et al. Kinetics of vascular normalization by VEGFR2 blockade governs brain tumor response to radiation: role of oxygenation, angiopoietin-1, and matrix metalloproteinases. *Cancer Cell*. 2004;6(6):553–563.
16. Allen M, Bjerke M, Edlund H, Nelander S, Westermark B. Origin of the U87MG glioma cell line: Good news and bad news. *Sci Transl Med*. 2016;8(354):354re3.
17. Keunen O, et al. Anti-VEGF treatment reduces blood supply and increases tumor cell invasion in glioblastoma. *Proc Natl Acad Sci U S A*. 2011;108(9):3749–3754.
18. Xu J, Wang J, Xu B, Ge H, Zhou X, Fang JY. Colorectal cancer cells refractory to anti-VEGF treatment are vulnerable to glycolytic blockade due to persistent impairment of mitochondria. *Mol Cancer Ther*. 2013;12(5):717–724.
19. Li L, et al. The importance of GLUT3 for de novo lipogenesis in hypoxia-induced lipid loading of human macrophages. *PLoS One*. 2012;7(8):e42360.
20. Maher F, Davies-Hill TM, Lysko PG, Henneberry RC, Simpson IA. Expression of two glucose transporters, GLUT1 and GLUT3, in cultured cerebellar neurons: Evidence for neuron-specific expression of GLUT3. *Mol Cell Neurosci*. 1991;2(4):351–360.
21. Vannucci SJ, Maher F, Simpson IA. Glucose transporter proteins in brain: delivery of glucose to neurons and glia. *Glia*. 1997;21(1):2–21.
22. Boado RJ, Black KL, Pardridge WM. Gene expression of GLUT3 and GLUT1 glucose transporters in human brain tumors. *Brain Res Mol Brain Res*. 1994;27(1):51–57.
23. Masin M, et al. GLUT3 is induced during epithelial-mesenchymal transition and promotes tumor cell proliferation in non-small cell lung cancer. *Cancer Metab*. 2014;2:11.

24. Flavahan WA, et al. Brain tumor initiating cells adapt to restricted nutrition through preferential glucose uptake. *Nat Neurosci*. 2013;16(10):1373–1382.

25. Le Calvé B, et al. Long-term in vitro treatment of human glioblastoma cells with temozolomide increases resistance in vivo through up-regulation of GLUT transporter and aldo-keto reductase enzyme AKR1C expression. *Neoplasia*. 2010;12(9):727–739.

26. Kitagawa T, Tsuruhara Y, Hayashi M, Endo T, Stanbridge EJ. A tumor-associated glycosylation change in the glucose transporter GLUT1 controlled by tumor suppressor function in human cell hybrids. *J Cell Sci*. 1995;108(Pt 12):3735–3743.

27. Zhao Y, Butler EB, Tan M. Targeting cellular metabolism to improve cancer therapeutics. *Cell Death Dis*. 2013;4:e532.

28. Pelicano H, Martin DS, Xu RH, Huang P. Glycolysis inhibition for anticancer treatment. *Oncogene*. 2006;25(34):4633–4646.

29. Bustin SA. *A-Z of Quantitative PCR*. La Jolla, CA: International University Line; 2004.

30. Ward CS, et al. Noninvasive detection of target modulation following phosphatidylinositol 3-kinase inhibition using hyperpolarized 13C magnetic resonance spectroscopy. *Cancer Res*. 2010;70(4):1296–1305.

31. Mehlem A, Hagberg CE, Muhl L, Eriksson U, Falkevall A. Imaging of neutral lipids by oil red O for analyzing the metabolic status in health and disease. *Nat Protoc*. 2013;8(6):1149–1154.

32. Koliwad SK, et al. Angiopoietin-like 4 (ANGPTL4, fasting-induced adipose factor) is a direct glucocorticoid receptor target and participates in glucocorticoid-regulated triglyceride metabolism. *J Biol Chem*. 2009;284(38):25593–25601.